Ohm's Law Survives to the Atomic Scale

B. Weber *et al.*

Science **335**, 64 (2012);
DOI: 10.1126/science.1214319

Science (print ISSN 0036-8075; online ISSN 1095-9203) is published weekly, except the last week in December, by the American Association for the Advancement of Science, 1200 New York Avenue NW, Washington, DC 20005.

14. P. E. Batson, *Nature* **366**, 727 (1993).
15. D. A. Muller, Y. Tzou, R. Raj, J. Silcox, *Nature* **366**, 725 (1993).
16. K. Suenaga *et al.*, *Science* **290**, 2280 (2000).
17. M. Varela *et al.*, *Phys. Rev. Lett.* **92**, 095502 (2004).
18. K. Kimoto *et al.*, *Nature* **450**, 702 (2007).
19. J. Nelayah *et al.*, *Nat. Phys.* **3**, 348 (2007).
20. A. Yurtsever, M. Couillard, D. A. Muller, *Phys. Rev. Lett.* **100**, 217402 (2008).
21. A. H. Zewail, *Science* **328**, 187 (2010).
22. A. H. Zewail, J. M. Thomas, *4D Electron Microscopy* (Imperial College Press, London, 2009).
23. A. Yurtsever, A. H. Zewail, *Science* **326**, 708 (2009).
24. A. Yurtsever, A. H. Zewail, *Proc. Natl. Acad. Sci. U.S.A.* **108**, 3152 (2011).
25. V. Ortalan, A. H. Zewail, *J. Am. Chem. Soc.* **133**, 10732 (2011).
26. B. Barwick, D. J. Flannigan, A. H. Zewail, *Nature* **462**, 902 (2009).
27. F. J. García de Abajo, A. Asenjo-Garcia, M. Kociak, *Nano Lett.* **10**, 1859 (2010).
28. S. T. Park, M. M. Lin, A. H. Zewail, *New J. Phys.* **12**, 123028 (2010).
29. A. Howie, *Eur. Phys. J. Appl. Phys.* **54**, 33502 (2011).
30. In general, the peaks of gain and loss for different photon quanta are well separated in energy in the raw data, but for quantification of intensities we applied the Richardson-Lucie deconvolution algorithm, which enabled use of the ZLP profile at negative time to quantify the evolution of peaks at each positive time.
31. N. Yamamoto, K. Araya, F. J. García de Abajo, *Phys. Rev. B* **64**, 205419 (2001).
32. In diffraction, beyond the one-electron kinematical regime, different Bragg peaks can exhibit a correlation in intensities depending on the strength of the projected Coulomb potential, leading to a complex behavior. In other words, because of multiple electron scattering, the intensities of different Bragg peaks essentially become interactive, with an increase in the intensity for some peaks and a decrease in others, depending on the specimen and its thickness.

Acknowledgments: Supported by NSF grant DMR-0964886 and Air Force Office of Scientific Research grant FA9550-11-1-0055 to the Gordon and Betty Moore Center for Physical Biology at the California Institute of Technology. R.M.V. was supported by the Swiss National Science Foundation. We thank S. T. Park for helpful discussions regarding the theoretical calculations.

Supporting Online Material

www.sciencemag.org/cgi/content/full/335/6064/59/DC1
Materials and Methods
Movies S1 to S3

2 September 2011; accepted 19 October 2011
10.1126/science.1213504

Ohm's Law Survives to the Atomic Scale

B. Weber,[1] S. Mahapatra,[1] H. Ryu,[2]* S. Lee,[2] A. Fuhrer,[1]† T. C. G. Reusch,[1] D. L. Thompson,[1] W. C. T. Lee,[1] G. Klimeck,[2] L. C. L. Hollenberg,[3] M. Y. Simmons[1]‡

As silicon electronics approaches the atomic scale, interconnects and circuitry become comparable in size to the active device components. Maintaining low electrical resistivity at this scale is challenging because of the presence of confining surfaces and interfaces. We report on the fabrication of wires in silicon—only one atom tall and four atoms wide—with exceptionally low resistivity (~0.3 milliohm-centimeters) and the current-carrying capabilities of copper. By embedding phosphorus atoms within a silicon crystal with an average spacing of less than 1 nanometer, we achieved a diameter-independent resistivity, which demonstrates ohmic scaling to the atomic limit. Atomistic tight-binding calculations confirm the metallicity of these atomic-scale wires, which pave the way for single-atom device architectures for both classical and quantum information processing.

The continuous miniaturization (*1*–*3*) of classical as well as quantum electronic devices and circuitry for information processing relies on the implementation of low-resistivity leads and interconnects that are of the same scale as the active device components themselves (*4*, *5*). At the fundamental limit of downscaling in semiconductor devices, functionality is obtained from only a few (*6*), or even single, dopant atoms (*7*–*9*) embedded within the semiconductor crystal. This emerging field of research, in which device properties are determined by a single dopant, is called solotronics (solitary dopant optoelectronics) (*10*). However, large-scale device architectures using multiple solitary dopants, such as donor-based quantum computers (*11*–*14*), require addressability of the individual dopants with interconnects comparable in size to the single-dopant Bohr radii (a_B ~ 2.5 nm for P in Si). In this size regime, maintaining low resistivity is challenging because of the increased ratio of surface or interface to volume that limits both the mobility and availability of free carriers. Indeed, in the sub-10-nm size regime, even heavily doped Si wires become highly resistive because of the limited doping density achievable (*15*) or as a result of the reduced doping efficiency (*16*) from the dielectric mismatch between the wire and its surroundings.

We demonstrate that bulk-like resistivities can be retained to the atomic scale by fabricating "interface-free" dopant wires embedded in single-crystalline Si. We used scanning probe lithography (*6*, *17*) and a gaseous dopant source to write atomic-scale dopant wires on the Si(100) surface. We then embedded them within the Si bulk using molecular beam epitaxy (MBE), thereby removing them from surface and interface states. Figure 1A shows a scanning tunneling microscopy (STM) image of a 1.5-nm-wide wire template (corresponding to two dimer rows) extending

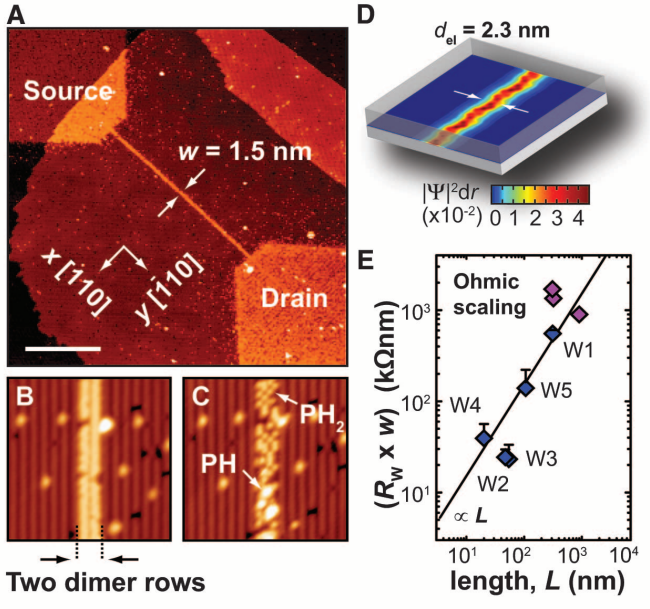

Fig. 1. Atomically abrupt dopant wires in silicon. (**A**) STM image of a 4-atom-wide (1.5 nm), one-atom-tall, and 106-nm-long wire template, patterned along the <110> direction and connected to source/drain leads. Scale bar, 50 nm. (**B** and **C**) Atomic resolution images of a two-dimer-row-wide wire, before (B) and after (C) PH_3 dosing. After PH_3 exposure, the wire shows a large number of PH_x (x = 1,2) fragments, strictly confined within the patterned regions. (**D**) Atomistic NEMO modeling of the electron distribution in a 1.5-nm dopant wire demonstrating tight charge confinement with a spread of the wave function outside the lithographic width. (**E**) Four-terminal resistances corrected for series resistances and normalized with the lithographic width ($R_W \times w$), plotted versus wire length L (blue and purple diamonds).

[1]Centre for Quantum Computation and Communication Technology, School of Physics, University of New South Wales, Sydney, NSW 2052, Australia. [2]Network for Computational Nanotechnology, Birck Nanotechnology Center, Purdue University, West Lafayette, IN 47907, USA. [3]Centre for Quantum Computation and Communication Technology, School of Physics, University of Melbourne, Parkville, VIC 3010, Australia.

*Present address: Supercomputing Center, Korea Institute of Science and Technology Information, Daejeon 305-806, South Korea.

†Present address: IBM Research–Zurich, Säumerstrasse 4, 8803 Rüschlikon, Switzerland.

‡To whom correspondence should be addressed. E-mail: michelle.simmons@unsw.edu.au

to a length of 106 nm between the source and drain leads. The dark regions correspond to hydrogen-terminated Si(001), and the features with lighter contrast correspond to Si dangling bonds exposed by the STM-induced desorption of the hydrogen resist monolayer. Source and drain contact arms were also patterned by STM lithography in the same fabrication step, extending out to a total size of ~2 μm (length) by ~1 μm (width), which were used for ex situ alignment of metal contacts (*17*). Subsequent exposure to PH_3 gas selectively doped the wire template as well as the contact arms with a resolution set by the atomistic nature of the underlying reconstructed Si(001) surface. Atomic-resolution images of a two-dimer-row-wide template before and after dosing (Fig. 1, B and C) highlight the adsorption of PH_x ($x = 1, 2$) solely within the wire region. After a short anneal and epitaxial overgrowth, the P dopants were embedded in the silicon bulk forming Si-P bonds, resulting in an atomically abrupt doping profile (*18*, *19*) with extremely high planar doping density of ~0.25 monolayers ($N_D \sim 2 \times 10^{14}$ cm^{-2}) (*20*). In three dimensions (3D), this density corresponds to a value of ~10^{21} cm^{-3}, three orders of magnitude beyond the Mott metal-insulator transition. The average dopant separation is <1 nm, smaller than the Bohr radius of a single donor ($a_B \sim 2.5$ nm) (*21*). Consequently, the wires are crystalline, atomically abrupt, and expected to show metallic conduction.

The wires presented here are thin enough to allow a fully atomistic theoretical treatment using the tight-binding code NEMO-3D (*22*, *23*). We calculated the self-consistent charge-potential profiles of the wires, taking into account both the high density and discrete nature of the doping. The wires were represented by an infinite repetition of a supercell in the <110> direction, with the doping distribution matched to a doping density of 0.25 ML for each lithographic linewidth. The modeled wires were embedded within 70 nm of silicon in both transverse directions. The central 16 nm was modeled with an atomistic representation of the silicon lattice, while the remaining 54 nm was represented as a homogeneous dielectric with $\varepsilon_{Si} = 11.7$. The density of states (DOS) was computed over the first Brillouin zone in 1D k-space, subject to charge neutrality in equilibrium, where the total electron number equals the number of positively ionized donors. Exchange and correlation effects are taken into account within the local density approximation (LDA) (*24*). The resultant electronic charge distribution along the thinnest wire (1.5 nm wide) is shown in Fig. 1D. The doping density changes by ~6 orders of magnitude from inside the wire ($N_D \sim 10^{21}$ cm^{-3}) to the lightly doped surrounding silicon substrate (~10^{15} cm^{-3}), giving an extremely small Thomas-Fermi screening length (~0.5 nm) and strong charge confinement.

Five different wires were measured (Table 1), all showing ohmic current-voltage (*I-V*) characteristics at $T = 4.2$ K. At an applied bias of 500 μV (a low value was chosen to avoid electromigration damage), we achieved current densities of up to 5×10^5 A cm^{-2}, which is near the maximum current densities of state-of-the-art copper interconnects (~10^6 A cm^{-2}) (*5*). To calculate the net wire resistance R_W, we first subtracted series resistances from the four-terminal resistances, which can be accurately determined by knowing both the sheet resistivity (530 Ω/□) and the exact geometry of each STM-patterned contact arm. Linear *I-V* characteristics with R_W <100 kΩ demonstrate the effective metallic doping down to a width of 1.5 nm. In Fig. 1E, we plot the wire resistance normalized by the lithographic width ($R_W \times w$) as a function of the wire length *L*. We include data from previously published results on wider STM-patterned wires (*25*) (purple diamonds) and observe ohmic scaling of the resistance for all devices, as typically observed in macroscopic metallic systems.

The unambiguous demonstration of ohmic scaling is a constant resistivity $\rho_W = R_W(A_{el}/L)$, independent of geometric variables such as wire length or width. When determining the resistivity of these wires, it is necessary to consider the effective electronic cross-sectional area, A_{el}, rather than their lithographic dimensions. Charge confinement is provided solely by the presence of the ionized dopants screened by both the silicon dielectric and the mobile electronic charge. As a consequence, the electronic width of the wire can extend into the surrounding silicon bulk and enlarge the effective diameter of the wire. The charge self-consistent NEMO-3D code captured this effect and allowed us to quantify A_{el} directly. Figure 2A shows the modeled radial charge distribution of the thinnest wire (W5), averaged over the length of the supercell. The decay of the charge distribution is given by $|\psi|^2\, dr$, where $\psi \sim \exp(-r/a)$ represents the electronic wave function away from the core region of the doped wire

Table 1. Atomic dopant wires of different width. *L* and *w* denote the lithographic length and width of each wire studied. A_{el} and d_{el} are the effective electronic cross section and diameter of the wires as determined by atomistic calculations. Resistivities, ρ_W, were extracted from the wire resistance R_W using A_{el}. Measured wire resistances are compared to theoretically predictions R_{calc} based on the tight-binding calculations.

Sample	*w* (nm)	*L* (nm)	A_{el} (nm^2)	d_{el} (nm)	R_W (kΩ)	ρ_W (mΩ cm)	R_{calc} (kΩ)
W1	11.0	312	27.5	13.1	48.6	0.43	30 ± 4
W2	4.6	47	9.8	5.2	5.3	0.11	7 ± 1
W3	2.3	54	5.0	2.9	10.1	0.10	15 ± 2
W4	2.3	20	5.0	2.9	17.1	0.42	6 ± 1
W5	1.5	106	3.8	2.3	82.3	0.26	31 ± 4

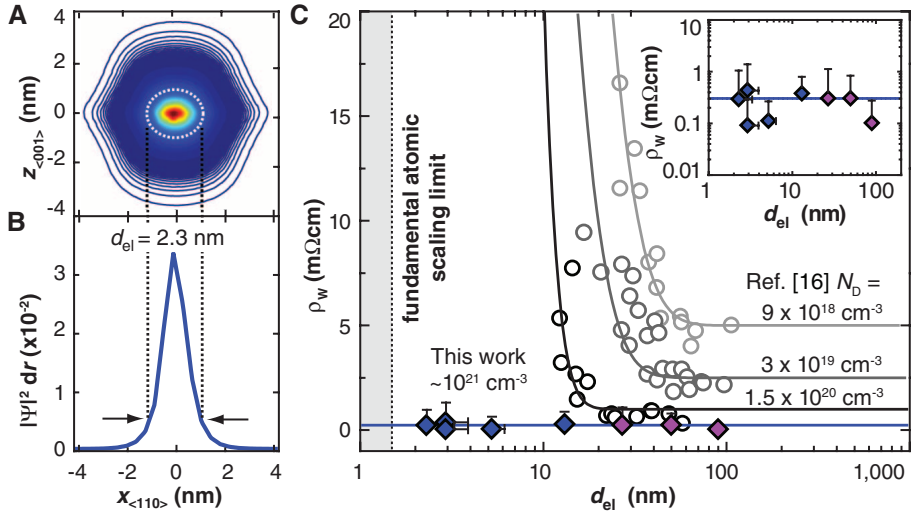

Fig. 2. Diameter-independent bulk-like resistivity down to the atomic limit. (**A**) Radial charge density $|\psi|^2\, dr$ of the thinnest wire (W5) showing the effective cross-sectional area A_{el} (white dotted ellipse), used to calculate the wire resistivity ρ_W. (**B**) The corresponding effective wire diameter d_{el} (arrows) is determined from a cut through $|\psi|^2\, dr$ in the plane of the dopants. (**C**) Resistivity ρ_W (d_{el}) of the STM-patterned wires (blue and purple diamonds), showing that it remains constant down to the fundamental scaling limit. The average value is near that for the silicon bulk resistivity at equivalent doping density (blue line). This is in contrast to an exponential deviation from bulk values as found in VLS-grown nanowires. [Open circles, data graphically extracted from (*16*). The lines are guides to the eye.] (Inset) ρ_W (d_{el}) on a double-logarithmic scale.

with a decay length a defined analogously to the Bohr radius a_B of an isolated P donor. By considering a in all radial directions, we quantify A_{el}, where ψ decays to 1/e of its peak value, as shown by the dotted line in Fig. 2A. Thus, >70% of the total electronic charge is enclosed in the modeling domain. In turn, this also allowed us to determine the effective electronic diameter d_{el} of the wire (arrows in Fig. 2B). For W5, we found d_{el} = 2.3 nm compared with w = 1.5 nm (see Table 1). We simulated several supercell configurations with different dopant positioning within the wire, which revealed negligible impact on either A_{el} or d_{el} down to the thinnest wire.

In Fig. 2C, we compare the resistivity ρ_W as a function of the wire diameter d_{el} (blue and purple diamonds) with reported values for other silicon wires. It is evident that for the STM-patterned wires, ρ_W remains constant despite d_{el} varying over nearly two orders of magnitude. The inset shows ρ_W on a double-logarithmic scale, revealing a minimum resistivity of 0.1 mΩ cm (W3), the lowest reported in doped silicon wires. The average resistivity (ρ_W = 0.3 ± 0.2 mΩ cm) is comparable to that of bulk-doped silicon of similar doping density (*26*) (blue line). The relatively large spread of resistivity at such low values can arise from sample-to-sample variations in the spatial distribution of the dopants within the wires. Our data contrasts sharply with the behavior of other doped Si wires previously reported, where strong deviations from bulk values of the resistivity were typically observed below d ~ 10 nm (*15*, *16*). We have reproduced the resistivity data of vapor-liquid-solid (VLS)–grown wires with three different doping densities, measured by Björk *et al.* (*16*), where the resistivity is observed to increase exponentially with decreasing diameter. This resistivity increase was more pronounced for the lower doping densities and prevailed even when the wire and resistivities were corrected for a depletion width arising from surface and interface states. Björk *et al.* attribute this exponential rise to suppression of dopant activation and a concomitant decrease in free-carrier density. Theoretical calculations by Diarra *et al.* (*27*) predict a d^{-1} dependence of dopant ionization energy for d < 10 nm, induced by a mismatch in the dielectric constants of the silicon wire (ε_{in}) and its environment (ε_{out}). For $\varepsilon_{in} > \varepsilon_{out}$, the dopant core potential is insufficiently screened, resulting in an increase in ionization energy. The exponential divergence persists to the highest doping density achievable in VLS growth (*15*), indicating the existence of a scaling barrier at d ~ 10 nm for doped silicon wires.

In contrast, by embedding the doped wires within bulk silicon, we eliminated the dielectric mismatch ($\varepsilon_{in} = \varepsilon_{out}$) and thereby achieved full dopant activation. This feature, combined with atomically doping the silicon wire to extremely high densities using a gaseous dopant source, allowed us to overcome the apparent scaling barrier and resulted in the persistence of bulk-like resistivity down to d_{el} = 2.3 nm (w = 1.5 nm).

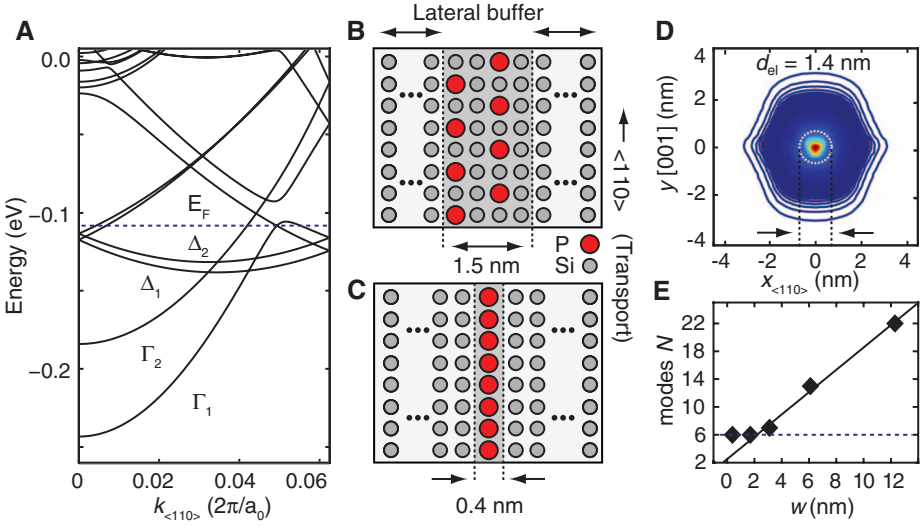

Fig. 3. Atomic-scale dopant wires at the scaling limit. (**A**) Band structure of the 1.5-nm-wide wire (W5) displaying band metallicity with six propagating modes (N = 6) at E_F = 135 meV, measured from the Γ_1 minimum. (**B** and **C**) Supercell configuration for the 1.5-nm-wide wire (B), as well as a single atomic chain of dopants (C) used to calculate the charge-potential profiles and band structures. (**D**) Radial charge distribution of a single atomic chain, representing the fundamental scaling limit for dopant wires in silicon. While maintaining N = 6, the electronic diameter d_{el} = 1.4 nm represents the fundamental scaling limit for dopant wires in silicon. (**E**) The number of modes N at the Fermi energy as a function of wire width w used to calculate wire resistances R_{calc}.

One of the advantages of atomistic tight-binding modeling is that we can determine the number of propagating metallic modes at the Fermi energy for different wire widths and from this estimate the resistance of the narrowest conducting STM-patterned doped wires in silicon. Figure 3A shows the self-consistent band structure calculation for the narrowest STM-patterned wire W5 (1.5 nm) based on the supercell configuration shown in Fig. 3B. We observed strong band bending, so that the minimum of the lowest occupied band (Γ_1) lies 243 meV below the conduction band edge of bulk silicon (E = 0). The Fermi energy E_F, indicated by the blue dotted lines, is situated well above the Γ_1 minimum (135 meV), making the wire a band-metal at T = 4.2 K. For this heavily doped silicon system, we observed occupation of the lowest sub-band in all six valleys of the Si conduction band, whose degeneracy is lifted by the strong vertical and lateral quantum confinement of the wires, giving N = 6 propagating modes at E_F (*6*, *21*).

We determined the number of modes in these doped silicon wires as we dropped the lithographic width down to an ideal single chain of individual dopants, represented by the supercell configuration in Fig. 3C. Below w ~ 2 nm, we observed a saturation of the number of propagating modes at E_F (N = 6), again reflecting the six conduction band valleys in silicon (Fig. 3E). The knowledge of $N(w)$, along with estimates of the electron mean free path in Si:P δ-doped systems (l = 8 ± 1 nm) (*28*), allowed us to calculate the resistance $R_{calc} = (h/2e^2N)(1 + L/l)$ in the diffusive regime of a multimode quasi-1D metal, where ($L >> l$) (*29*). We obtained good agreement with resistances obtained experimentally for all wires, as shown in Table 1. Small deviations could be explained by sample-to-sample fluctuations of the conductance (*30*), expected in the diffusive regime and the potential onset of electron localization at low temperature (*29*) not captured in this model. We also determined the absolute physical limit to which doped silicon wires could be scaled and found the radial charge distribution of a single dopant chain to be ~1.4 nm (Fig. 3D). This number therefore defines the fundamental atomic scaling limit (vertical line in Fig. 2C) of doped silicon wires.

These STM-patterned wires achieve charge confinement in the absence of any surface or material interface. The combination of extremely high doping density and atomically abrupt dopant positioning in a crystalline environment provides an unprecedented scalability to atomic-scale dimensions, yet retains a diameter-independent, bulk-like resistivity. The resulting persistence of Ohm's law at the atomic limit paves the way for ultrascaled classical as well as quantum electronic components, such as source-drain leads, interconnects, and local electrostatic gates necessary to electrically address individual dopants in solotronic and donor-based quantum computing architectures.

References and Notes

1. M. Ieong, B. Doris, J. Kedzierski, K. Rim, M. Yang, *Science* **306**, 2057 (2004).
2. M. Lundstrom, *Science* **299**, 210 (2003).
3. E. Vogel, *Nat. Nanotechnol.* **2**, 25 (2007).
4. J. D. Meindl, Q. Chen, J. A. Davis, *Science* **293**, 2044 (2001).
5. ITRS Roadmap, 2009 edition, available from http://public.itrs.net.

6. M. Fuechsle *et al.*, *Nat. Nanotechnol.* **5**, 502 (2010).
7. G. P. Lansbergen *et al.*, *Nat. Phys.* **4**, 656 (2008).
8. M. Pierre *et al.*, *Nat. Nanotechnol.* **5**, 133 (2010).
9. A. Morello *et al.*, *Nature* **467**, 687 (2010).
10. P. M. Koenraad, M. E. Flatté, *Nat. Mater.* **10**, 91 (2011).
11. B. E. Kane, *Nature* **393**, 133 (1998).
12. R. Vrijen *et al.*, *Phys. Rev. A* **62**, 012306 (2000).
13. C. D. Hill *et al.*, *Phys. Rev. B* **72**, 045350 (2005).
14. L. C. L. Hollenberg, A. D. Greentree, A. G. Fowler, C. J. Wellard, *Phys. Rev. B* **74**, 045311 (2006).
15. V. Schmidt, J. V. Wittemann, S. Senz, U. Gösele, *Adv. Mater.* **21**, 2681 (2009).
16. M. T. Björk, H. Schmid, J. Knoch, H. Riel, W. Riess, *Nat. Nanotechnol.* **4**, 103 (2009).
17. A. Fuhrer, M. Füchsle, T. C. G. Reusch, B. Weber, M. Y. Simmons, *Nano Lett.* **9**, 707 (2009).
18. L. Oberbeck, N. J. Curson, T. Hallam, M. Y. Simmons, R. G. Clark, *Thin Solid Films* **464-465**, 23 (2004).
19. F. J. Ruess *et al.*, *Small* **3**, 563 (2007).
20. S. R. McKibbin, W. R. Clarke, A. Fuhrer, T. C. G. Reusch, M. Y. Simmons, *Appl. Phys. Lett.* **95**, 233111 (2009).
21. G. Qian, Y.-C. Chang, J. R. Tucker, *Phys. Rev. B* **71**, 045309 (2005).
22. G. Klimeck *et al.*, *IEEE Trans. Electron. Dev.* **54**, 2090 (2007).
23. S. Lee, H. Ryu, Z. Jiang, G. Klimeck, 13th International Workshop on Computational Electronics, Beijing, 27 to 29 May 2009 (2009), pp. 1–4.
24. E. Gawlinski, T. Dzurak, R. A. Tahir-Kheli, *J. Appl. Phys.* **72**, 3562 (1992).
25. F. J. Ruess *et al.*, *Nanotechnology* **18**, 044023 (2007).
26. A. Yamada, Y. Jia, M. Konagai, K. Takahashi, *Jpn. J. Appl. Phys.* **28**, L2284 (1989).
27. M. Diarra, Y.-M. Niquet, C. Delerue, G. Allan, *Phys. Rev. B* **75**, 045301 (2007).
28. K. E. J. Goh, L. Oberbeck, M. Y. Simmons, A. R. Hamilton, M. J. Butcher, *Phys. Rev. B* **73**, 035401 (2006).
29. C. W. J. Beenakker, *Rev. Mod. Phys.* **69**, 731 (1997).
30. P. A. Lee, A. D. Stone, *Phys. Rev. Lett.* **55**, 1622 (1985).

Acknowledgments: This research was conducted by the Australian Research Council Centre of Excellence for Quantum Computation and Communication Technology (project number CE110001027) and the US National Security Agency and the US Army Research Office under contract number W911NF-08-1-0527. M.Y.S. acknowledges an ARC Federation Fellowship and support from the Semiconductor Research Corporation. L.H. is supported under an ARC Professorial Fellowship. National Science Foundation (NSF) supported nanoHUB.org computational resources, TeraGrid resources provided by the National Institute for Computational Sciences (NICS) and the Texas Advanced Computed Center (TACC) computational resources have been extensively used in this work. The authors declare that they have no competing financial interests.

22 September 2011; accepted 11 November 2011
10.1126/science.1214319

Candle Soot as a Template for a Transparent Robust Superamphiphobic Coating

Xu Deng,[1,2] Lena Mammen,[1] Hans-Jürgen Butt,[1] Doris Vollmer[1]*

Coating is an essential step in adjusting the surface properties of materials. Superhydrophobic coatings with contact angles greater than 150° and roll-off angles below 10° for water have been developed, based on low-energy surfaces and roughness on the nano- and micrometer scales. However, these surfaces are still wetted by organic liquids such as surfactant-based solutions, alcohols, or alkanes. Coatings that are simultaneously superhydrophobic and superoleophobic are rare. We designed an easily fabricated, transparent, and oil-rebounding superamphiphobic coating. A porous deposit of candle soot was coated with a 25-nanometer-thick silica shell. The black coating became transparent after calcination at 600°C. After silanization, the coating was superamphiphobic and remained so even after its top layer was damaged by sand impingement.

A major goal in coating research is to design self-cleaning surfaces (*1*–*4*). Many surfaces in nature are superhydrophobic; for example, lotus leaves (*5*). Mimicking their surface morphology led to the development of a number of artificial superhydrophobic surfaces (*6*, *7*), opening many applications in industrial and biological processes (*8*–*13*). Microscopic pockets of air are trapped beneath the water drops (*14*–*17*). This composite interface leads to an increase in the macroscopic contact angle and a reduced contact angle hysteresis, enabling water drops to roll off easily, taking dirt with them. However, the addition of an organic liquid such as alcohol or oil decreases the interfacial tension sufficiently to induce homogeneous wetting of the surface. Drops, initially resting on air pockets (in a Cassie state), pass the transition to complete wetting (a Wenzel state) (*14*). No naturally occurring surface is known to show a contact angle θ greater than 150° and roll-off angles below 10° for water and organic liquids. These superhydrophobic and superoleophobic surfaces are called superamphiphobic (*18*).

In contrast to superhydrophobicity, the term "superamphiphobicity" is not uniquely defined, in particular with respect to the liquid used (*19*–*22*). According to Young's equation, $\cos\Theta = (\gamma_{SV} - \gamma_{SL})/\gamma_{LV}$, the lower the surface tension, the higher the tendency of a liquid to spread on a solid surface (*22*, *23*). Here, Θ is the macroscopic contact angle, γ_{SV} is the surface tension of the solid, and γ_{SL} is the interfacial tension of the solid/liquid interface. For organic liquids ($30 \leq \gamma_{LV} \leq 18$ mN/m), mainly van der Waals interactions act between the molecules. Therefore, $\gamma_{SV} - \gamma_{SL}$ is positive, and on planar surfaces $\Theta < 90°$. Similarly, the contact angle on rough surfaces depends on the surface tensions, because roughness amplifies the wetting properties.

The key factors for superamphiphobicity are not clear yet. For water repellency, surface roughness and low surface energy are essential (*14*). To fabricate superamphiphobic surface overhangs, reentrant geometry or convex curvature is also important (*19*–*25*). The complex interplay between surface roughness, low surface energy, and topography has made it difficult and expensive to fabricate superamphiphobic surfaces. Tuteja *et al*. showed that careful design of the topography of a surface allows the construction of surfaces with a contact angle for hexadecane close to 160°, although the flat surface was oleophilic (*19*, *23*). They explained their exceptional oil-repellency by overhang structures and reentrant geometry.

Here, we describe a simple way to make robust, transparent, superamphiphobic coatings. The surface to be coated, in our case a glass slide, is held above the flame of a paraffin candle (Fig. 1A). Deposition of a soot layer turns the glass black. Scanning electron microscopy reveals that the soot consists of carbon particles with a typical diameter of 30 to 40 nm, forming a loose, fractal-like network (Fig. 1, B and C) (*26*). A water drop gently deposited on the surface shows a contact angle above 160° and rolls off easily, demonstrating the surface's superhydrophobicity (*27*). However, the structure is fragile because the particle-particle interactions are only physical and are weak. When water rolls off the surface, the drop carries soot particles with it until almost all of the soot deposit is removed and the drop undergoes a wetting transition (movie S1).

Inspired by the promising morphology of soot, we developed a technique to coat the soot layer with a silica shell, making use of chemical vapor deposition (CVD) of tetraethoxysilane (TES) catalyzed by ammonia. The soot-coated substrates were placed in a desiccator together with two open glass vessels containing TES and ammonia, respectively (fig. S1). Similar to a Stöber reaction, silica is formed by hydrolysis and condensation of TES. The shell thickness can be tuned by the duration of CVD. After 24 hours, the particles were coated by a 20 ± 5–nm–thick silica shell (Fig. 1, D and E). Calcinating the

[1]Max Planck Institute for Polymer Research, Ackermannweg 10, D-55128, Mainz, Germany. [2]Center of Smart Interfaces, Technical University Darmstadt, 64287 Darmstadt, Germany.

*To whom correspondence should be adddressed. E-mail: vollmerd@mpip-mainz.mpg.de